Mild UV–X-Ray Slope Evolution Collapses Apparent Extreme High-Redshift Distance Compression in Unified-Flow Quasar Cosmography

Jason Yancey *

Posted Date: 20 March 2026

doi: 10.20944/preprints202603.1595.v1

Keywords: cosmological distances; quasars; Type Ia supernovae; UV–X-ray relation; model identifiability; cross-validation; varying constants

 doi:10.20944/preprints202603.1595.v1

Article

Mild UV–X-Ray Slope Evolution Collapses Apparent Extreme High-Redshift Distance Compression in Unified-Flow Quasar Cosmography

Jason Yancey

Independent Researcher, USA; jasonyancey@yanceyconsult.com

Abstract

A joint analysis of Pantheon+SH0ES Type Ia supernovae and a 2421-object quasar UV–X-ray catalog is presented within the Unified-Flow distance-scaling framework. The core hypothesis tested is that a mild, monotonic redshift evolution in the quasar UV–X-ray slope can absorb the apparent high-redshift residual drift that otherwise drives an extreme Unified-Flow distance-law transition. The Unified-Flow specification provides a mapping between a redshift-dependent scaling field and the luminosity-distance integral, while the quasar likelihood constrains the same distance through a non-linear UV–X-ray flux relation. Four nested model classes are compared: single- and two-regime distance laws, each combined with either a constant quasar UV–X-ray slope or a minimal redshift evolution of that slope. When the quasar slope is forced constant, the best fit drives the high-redshift distance-law exponent to an extreme value and yields strong compression of inferred distances above redshift unity. Allowing mild slope evolution removes the high-redshift residual drift that motivates the extreme branch and collapses the preferred distance-law transition to an order-unity regime. A leakage-controlled low-redshift calibration and multiple cross-validation schemes support the interpretation that an apparent extreme high-redshift distance transition is not robust to admitting small, monotonic evolution in quasar standardization. Quantitative predictions are stated for independent quasar catalogs and future high-redshift distance indicators.

Keywords: cosmological distances; quasars; Type Ia supernovae; UV–X-ray relation; model identifiability; cross-validation; varying constants

1. Introduction

Unified-Flow cosmography specifies a redshift-dependent scaling field $\phi(z)$ that modifies the luminosity-distance integral through coupled scalings of an effective expansion-rate factor and an effective light speed, with likelihood machinery for full-covariance supernova Hubble-diagram inference and analytic nuisance profiling defined by Yancey [1]. Type Ia supernovae provide a low-redshift distance anchor through empirical standardization of light-curve width and color, beginning with the decline-rate relation [2] and subsequent two-parameter formulations [3], with modern light-curve models and large compilations enabling precision Hubble-diagram inference [4–6]. The Pantheon+ release and its SH0ES calibration supply a 1701-object Hubble-diagram table with a full statistical-plus-systematic covariance matrix [7–9].

High-redshift supernova Hubble-diagram analyses historically established accelerated expansion through standardized Type Ia distances [10,11].

Quasars extend distance-like information to redshifts above those of supernova compilations through the observed correlation between ultraviolet and X-ray emission from accretion discs and coronae [12,13]. In the disc–corona picture, thermal optical/UV photons produced by the accretion disc supply the seed radiation field for inverse-Compton up-scattering in a hot corona, so both bands trace the same underlying accretion flow and its division of power between disc and corona. Broadband

 doi:10.20944/preprints202603.1595.v1

quasar spectral-energy distributions and extreme-ultraviolet spectral properties establish the physical context for UV and X-ray monochromatic measurements [14–16]. Empirically, the optical/UV–to–X-ray slope and its dependence on luminosity and redshift have been studied across wide samples [17–20]. A tight relation between X-ray and UV luminosities has been proposed as the basis for a quasar Hubble diagram [21,22], with high-redshift quasar Hubble-diagram analyses reporting departures from the concordance ΛCDM distance–redshift relation at $z \gtrsim 1.5$ [23] and a large, homogenized UV–X-ray catalog enabling systematic treatments of selection and calibration [24]. Independent investigations have examined the reliability and spectroscopic stability of the UV–X-ray method at high redshift [25–28] and have developed alternative calibration strategies, including model-independent approaches [29,30] and comparative studies that find shorter quasar-inferred luminosity distances than other high-redshift indicators [31].

A concise contextual comparison to the standard cosmological model is useful because ΛCDM distances, when fixed by external constraints, provide a well-defined reference curve. Cosmological-parameter constraints from Planck 2018 [32] and baryon acoustic oscillations [33,34] define a baseline for $\tilde{d}_L(z)$ up to high redshift, while reviews summarize current tensions between early- and late-Universe inferences [35,36]. Quasar Hubble-diagram studies have reported persistent high-redshift deviations from ΛCDM predictions [23,25,31]. That reference curve is informative but not sufficient for the present identifiability problem: in a quasar Hubble diagram, a redshift-dependent mismatch can arise either from the cosmological distance law or from evolution in the quasar standardization itself.

Unified-Flow is adopted as a phenomenological distance-law framework precisely because it separates that question from a fixed dark-energy history. Rather than assuming a specific ΛCDM expansion history and treating residual quasar trends purely as systematics, the model parameterizes the distance law directly through the scaling field $\phi(z)$ and its logarithmic slope $\beta(z)$. Joint fits can therefore test whether the observed high-redshift compression is more parsimoniously described by a change in the distance law, by a change in the UV–X-ray slope, or by a combination of both.

Identifiability becomes central when quasars and supernovae are analyzed jointly. The quasar UV–X-ray standardization contains distance dependence through a coefficient proportional to $\gamma(z) - 1$, where γ is the UV–X-ray slope, while Unified-Flow distances depend on a distance-law evolution index $\beta(z) \equiv d\ln\phi/d\ln(1+z)$. A redshift-dependent change in $\gamma(z)$ can mimic a redshift-dependent change in $\tilde{d}_L(z)$, generating a degeneracy between quasar evolution and distance-law evolution. Quantifying that degeneracy, controlling calibration leakage from high to low redshift, and testing predictive robustness under held-out evaluation motivate the model set and diagnostics below.

Figure 1 summarizes the structure of that degeneracy at the level of the quasar likelihood.

 doi:10.20944/preprints202603.1595.v1

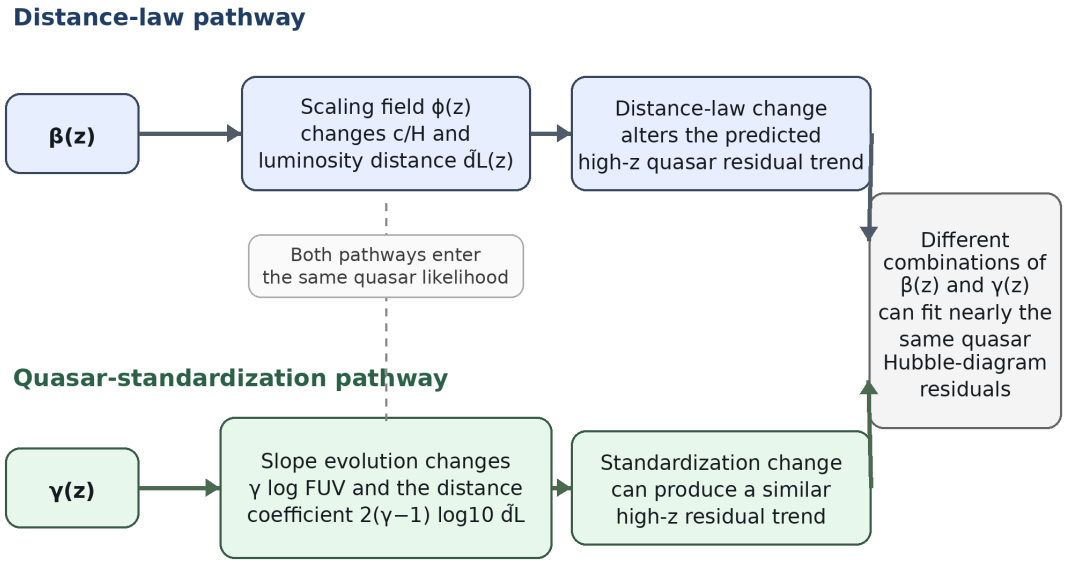

Figure 1. Conceptual schematic of the $\beta(z)$–$\gamma(z)$ degeneracy. The upper pathway shows how a change in the Unified-Flow distance-law index $\beta(z)$ propagates through the scaling field $\phi(z)$ into the luminosity distance $\tilde{d}_L(z)$ and therefore into the predicted quasar residual trend. The lower pathway shows how a change in the UV–X-ray slope $\gamma(z)$ alters both the direct $\gamma \log F_{\rm UV}$ term and the distance-coupling coefficient $2(\gamma-1)\log_{10}\tilde{d}_L$. Because both pathways enter the same quasar likelihood, mild evolution in $\gamma(z)$ can mimic part of an apparent redshift dependence in the distance law.

2. Materials and Methods

2.1. Data

Type Ia supernovae. The Pantheon+SH0ES compilation provides $N_{\rm SN} = 1701$ standardized Type Ia supernova distance moduli $\mu_{\rm SH0ES}$ with corresponding redshifts $z_{\rm HD}$ and the full STAT+SYS covariance matrix $\mathbf{C}_{\rm SN} \in \mathbb{R}^{1701\times1701}$ [7,9].

Quasars. The quasar sample was taken from Table 3 of Lusso et al. [24] and contains $N_{\rm QSO} = 2421$ objects spanning $z \in [0.009, 7.5413]$. The analysis used the tabulated redshift z, the base-10 logarithms of the monochromatic UV and X-ray flux densities ($\log F_{\rm UV}$ and $\log F_X$, in units of $\log(\mathrm{erg\ s^{-1}\ cm^{-2}\ Hz^{-1}})$), their reported measurement uncertainties ($\sigma_{\log F_{\rm UV}}$ and $\sigma_{\log F_X}$), and the catalog group label Group. No additional external datasets were introduced.

Table 3 of Lusso et al. is already a cleaned cosmological subsample rather than the raw parent catalog. The published construction homogenized the available optical/UV and X-ray measurements to rest-frame 2500 Å and 2 keV flux densities and applied quality cuts designed to suppress known biases in the UV–X-ray relation, including dust reddening and host-galaxy contamination, signatures of X-ray absorption, and sources vulnerable to flux-limit/Eddington bias. The present analysis intentionally introduced no further pruning so that all inference refers to the published 2421-object realization and remains directly comparable to earlier quasar Hubble-diagram studies.

The validity of that catalog for cosmological standardization is supported by follow-up spectroscopic checks showing that the adopted cosmological sample has low average reddening and limited host contamination, while the UV–X-ray relation remains stable enough for Hubble-diagram use once the published cleaning procedure is applied [27,28]. At the same time, systematic uncertainty is expected to grow toward the highest redshifts because rest-frame 2500 Å shifts into observed near-infrared bands, rest-frame 2 keV can require longer extrapolation from softer observed X-ray photons, and UV/X-ray measurements are generally non-simultaneous. Those effects are not modeled with

 doi:10.20944/preprints202603.1595.v1

separate nuisance fields in the present work; instead they enter through the catalog measurement uncertainties, the fitted intrinsic scatter $\sigma_{\rm int}$, and the held-out validation tests.

2.2. Unified-Flow Distance Scaling

The distance-scaling framework followed Yancey [1] as the governing specification for the mapping between the scaling field $\phi(z)$, the expansion-rate factor, and the luminosity-distance integral, and for the supernova likelihood and analytic profiling machinery.

A dimensionless scaling function $\phi(z)$ was defined with normalization $\phi(0) = 1$. It acts as a phenomenological bookkeeping field for departures of the effective propagation and expansion factors from their $z = 0$ normalization. The Unified-Flow evolution index was defined by

$$\beta(z) \equiv \frac{d\ln\phi(z)}{d\ln(1+z)}. \tag{1}$$

Operationally, $\beta(z)$ is the logarithmic redshift slope of the scaling field. Through Equations (2)–(4), it controls the quantity actually constrained by the data, namely the light-propagation factor $c(z)/H(z)$ and its integral $\tilde{d}_L(z)$. Positive β makes $\phi(z)$ grow with redshift, suppresses c/H at high z, and compresses luminosity distances; negative β has the opposite effect. In that sense, $\beta(z)$ plays a role analogous to the shape parameters entering standard-cosmology distance laws, but is defined directly from the phenomenological scaling field rather than from an assumed matter-plus-dark-energy decomposition.

The Unified-Flow mapping between $\phi(z)$, the Hubble factor, and the effective light speed followed Yancey [1]:

$$\frac{H(z)}{H_0} = (1+z)^{3/2}\phi(z)^{1/2}, \qquad \frac{c(z)}{c_0} = \phi(z)^{-1}. \tag{2}$$

The ratio entering the light-propagation integral therefore satisfied

$$\frac{c(z)}{H(z)} = \frac{c_0}{H_0}(1+z)^{-3/2}\phi(z)^{-3/2}. \tag{3}$$

The dimensionless luminosity distance was computed as

$$\tilde{d}_L(z) = (1+z)\int_0^z (1+z')^{-3/2}\phi(z')^{-3/2}\,dz'. \tag{4}$$

2.2.1. Constant-Beta Specialization

For constant β, $\phi(z) = (1+z)^{\beta}$, giving an integrand proportional to $(1+z)^{-\Gamma(\beta)}$ where

$$\Gamma(\beta) \equiv \frac{3}{2}(1+\beta) \tag{5}$$

following Yancey [1]. The corresponding closed-form distance [1] was evaluated as

$$\tilde{d}_L(z;\beta) = (1+z)\,\frac{(1+z)^{1-\Gamma(\beta)} - 1}{1-\Gamma(\beta)} \quad (\Gamma \neq 1), \tag{6}$$

with the continuous limit $\tilde{d}_L(z;\beta = -1/3) = (1+z)\ln(1+z)$.

2.2.2. Two-Regime Step Beta(z)

A two-regime step model was defined by

$$\beta(z) = \begin{cases} \beta_{\rm low}, & z \le z_t, \\ \beta_{\rm high}, & z > z_t, \end{cases} \tag{7}$$

 doi:10.20944/preprints202603.1595.v1

with $\phi(0) = 1$ and continuity at z_t enforced through

$$\phi(z) = \begin{cases} (1+z)^{\beta_{\text{low}}}, & z \le z_t, \\ (1+z_t)^{\beta_{\text{low}}-\beta_{\text{high}}}(1+z)^{\beta_{\text{high}}}, & z > z_t. \end{cases} \tag{8}$$

This yields a piecewise analytic $\tilde{d}_L$ obtained by splitting the integral at z_t. For numerical stability, the $\Gamma \to 1$ logarithmic limit was used when needed.

2.3. Supernova Distance-Modulus Model and Likelihood

For each supernova at redshift z_i, the modeled distance modulus followed Yancey [1]:

$$\mu_{\text{th}}(z_i;\theta) = 5\log_{10}\tilde{d}_L(z_i;\theta) + M, \tag{9}$$

where θ denotes the Unified-Flow distance-law parameter set of the model under consideration, and M is an additive nuisance offset absorbing the absolute magnitude and the overall scale c_0/H_0 [1]. The residual vector was

$$\Delta\boldsymbol{\mu} = \boldsymbol{\mu}_{\text{SH0ES}} - \boldsymbol{\mu}_{\text{th}}. \tag{10}$$

The full-covariance statistic was

$$\chi^2_{\text{SN}}(\theta, M) = \Delta\boldsymbol{\mu}^{\mathsf{T}}\mathbf{C}_{\text{SN}}^{-1}\Delta\boldsymbol{\mu}. \tag{11}$$

The covariance was whitened using a Cholesky factorization $\mathbf{C}_{\text{SN}} = \mathbf{L}\mathbf{L}^{\mathsf{T}}$, yielding whitened vectors $\mathbf{y} = \mathbf{L}^{-1}\Delta\boldsymbol{\mu}$ and $\chi^2_{\text{SN}} = \mathbf{y}^{\mathsf{T}}\mathbf{y}$ [1]. The linear nuisance parameter M was analytically profiled [1]:

$$M^*(\theta) = \frac{\mathbf{1}^{\mathsf{T}}\mathbf{C}_{\text{SN}}^{-1}\left(\boldsymbol{\mu}_{\text{SH0ES}} - 5\log_{10}\tilde{d}_L(\theta)\right)}{\mathbf{1}^{\mathsf{T}}\mathbf{C}_{\text{SN}}^{-1}\mathbf{1}}, \tag{12}$$

and the profiled supernova contribution $\chi^2_{\text{SN}}(\theta, M^*)$ was used for all fits.

2.4. Quasar UV–X-Ray Relation and Likelihood

The UV–X-ray standardization followed the flux-form relation adopted for the Lusso et al. quasar catalog. Throughout, log denotes $\log_{10}$ and ln denotes the natural logarithm:

$$\log F_X = \gamma(z)\,\log F_{\text{UV}} + 2\big(\gamma(z) - 1\big)\log_{10}\tilde{d}_L(z;\theta) + \kappa_F, \tag{13}$$

where γ is the UV–X-ray slope parameter and κ_F is an intercept absorbing constants (including the unknown absolute distance scale and unit conventions). The residual for object i was

$$r_i = \log F_{X,i} - \gamma(z_i)\log F_{\text{UV},i} - 2\big(\gamma(z_i) - 1\big)\log_{10}\tilde{d}_L(z_i;\theta) - \kappa_F. \tag{14}$$

Measurement errors and intrinsic scatter were combined in the variance model

$$s_i^2 = \sigma^2_{\log F_X,i} + \gamma(z_i)^2\,\sigma^2_{\log F_{\text{UV}},i} + \sigma^2_{\text{int}}, \tag{15}$$

where σ_{int} is a fitted intrinsic-scatter parameter in $\log F_X$. Assuming independent Gaussian residuals in $\log F_X$, the quasar contribution was taken as

$$-2\ln\mathcal{L}_{\text{QSO}}(\theta, \gamma, \sigma_{\text{int}}, \kappa_F) = \sum_i \left(\frac{r_i^2}{s_i^2} + \ln s_i^2\right) + \text{const.} \tag{16}$$

The intercept κ_F enters linearly and was analytically profiled at fixed $(\theta, \gamma, \sigma_{\text{int}})$ using weights $w_i = s_i^{-2}$:

$$\kappa_F^* = \frac{\sum_i w_i\, r_{0,i}}{\sum_i w_i}, \tag{17}$$

 doi:10.20944/preprints202603.1595.v1

where $r_{0,i}$ denotes the residual evaluated at $\kappa_F = 0$. The profiled value $-2\ln\mathcal{L}_{\rm QSO}(\kappa_F^*)$ was used for all fits.

2.5. Slope Evolution and Strict Low-Redshift Calibration

A minimal, testable evolution model was adopted:

$$\gamma(z) = \gamma_0 + \gamma_1 \ln(1+z), \tag{18}$$

using the natural logarithm. The constant-γ case is recovered at $\gamma_1 = 0$.

Strict low-redshift calibration was implemented as an explicit two-stage constraint intended to prevent high-redshift quasars from influencing the standardization slope:

1. **Calibration stage:** a low-redshift subset of quasars with $z \le 1.5$ was fit for $(\gamma, \sigma_{\rm int})$ or $(\gamma_0, \gamma_1, \sigma_{\rm int})$, using supernova-anchored distances $\tilde{d}_L(z)$ computed from the supernova-only best-fit constant-β Unified-Flow solution. The quasar intercept κ_F was profiled analytically.
2. **Inference stage:** the calibrated γ-parameters and $\sigma_{\rm int}$ were held fixed, and Unified-Flow distance-law parameters θ were fit using the full supernova likelihood together with the high-redshift quasar subset $z > 1.5$, while continuing to profile κ_F analytically within the inference subset.

2.6. Joint Likelihood and Model Sets

The joint objective followed Yancey [1] for the supernova component, augmented by the quasar likelihood:

$$-2\ln\mathcal{L}_{\rm tot}(\Theta) = \chi^2_{\rm SN}(\theta, M^*) + \left[-2\ln\mathcal{L}_{\rm QSO}(\theta, \gamma, \sigma_{\rm int}, \kappa_F^*)\right], \tag{19}$$

where Θ denotes the parameter set of a given model and (M, κ_F) are profiled at every likelihood evaluation.

Four nested model classes were fit and compared:

- **Model A:** constant β; constant γ; free $(\beta, \gamma, \sigma_{\rm int})$; profiled (M, κ_F).
- **Model B:** step $\beta(z)$ with $(\beta_{\rm low}, \beta_{\rm high}, z_t)$; constant γ; free $(\beta_{\rm low}, \beta_{\rm high}, z_t, \gamma, \sigma_{\rm int})$; profiled (M, κ_F).
- **Model C:** constant β; evolving $\gamma(z)$; free $(\beta, \gamma_0, \gamma_1, \sigma_{\rm int})$; profiled (M, κ_F).
- **Model D:** step $\beta(z)$; evolving $\gamma(z)$; free $(\beta_{\rm low}, \beta_{\rm high}, z_t, \gamma_0, \gamma_1, \sigma_{\rm int})$; profiled (M, κ_F).

2.7. Optimization, Uncertainty Estimation, and Model Comparison

One-dimensional supernova-only constant-β fits used bounded scalar minimization over $\beta \in [-1.5, 0.5]$. Multi-parameter optimizations used derivative-free Powell minimization [37] with tight termination tolerances (`xtol` $\approx 10^{-4}$–10^{-6}, `ftol` $\approx 10^{-4}$–10^{-6}) and multiple initializations to verify stability. The intrinsic scatter parameter was optimized in logarithmic space via the natural logarithm $\ln\sigma_{\rm int}$ to enforce positivity.

Uncertainties for single-parameter supernova-only fits were reported from the profile criterion $\Delta\chi^2 = 1$ [1]. For joint multi-parameter fits, 1σ uncertainties for the free parameters were computed from the local quadratic approximation of $-2\ln\mathcal{L}_{\rm tot}$ about the best fit, using a finite-difference Hessian $\mathbf{H}$ and covariance approximation $\mathrm{Cov} \approx 2\mathbf{H}^{-1}$. Reported uncertainties for $\sigma_{\rm int}$ were propagated from $\ln\sigma_{\rm int}$. Because M and κ_F were profiled analytically rather than included among the finite-difference Hessian coordinates, the reported uncertainties for those offsets are conditional profile standard errors evaluated at the best-fit free parameters: $\sigma_M = (\mathbf{1}^{\mathsf{T}}\mathbf{C}_{\rm SN}^{-1}\mathbf{1})^{-1/2}$ and $\sigma_{\kappa_F} = (\sum_i w_i)^{-1/2}$.

Nested likelihood-ratio tests used $\Delta(-2\ln\mathcal{L})$ with degrees of freedom set by the difference in parameter count, interpreted under the large-sample likelihood-ratio distribution [38]. In addition to the raw likelihood differences, the corresponding likelihood-ratio tail probabilities $p_{\rm LR}$ were evaluated from the $\chi^2_{\Delta k}$ survival function. Information criteria were reported as

$$\mathrm{AIC} = (-2\ln\mathcal{L}_{\rm min}) + 2k, \qquad \mathrm{BIC} = (-2\ln\mathcal{L}_{\rm min}) + k\ln N, \tag{20}$$

 doi:10.20944/preprints202603.1595.v1

with $N = N_{\rm SN} + N_{\rm QSO}$ and k counting all estimated parameters including analytically profiled (M, κ_F) and $\sigma_{\rm int}$ [39,40]. AIC is appropriate because it estimates the relative expected out-of-sample information loss of models fit to the same data vector, while BIC applies a stronger sample-size-dependent penalty and therefore guards more aggressively against over-interpreting additional parameters in a sample of more than four thousand objects. For regular large-sample models, ΔBIC also approximates $2\ln$ Bayes factors and therefore provides a compact evidence-scale summary without requiring explicit prior-volume choices [41]. Full Bayesian evidence integrals were not computed because the present analysis was formulated as a likelihood comparison; the BIC approximation was used instead as a transparent large-sample diagnostic.

Predictive robustness against overfitting was evaluated by leakage-free quasar cross-validation with the supernova likelihood retained in all training fits: (i) 10-fold random splits; (ii) 10 contiguous redshift blocks; and (iii) a high-redshift holdout with training on $z \leq 2.3$ and testing on $z > 2.3$ [42,43]. Test-set scores used the held-out quasar $-2\ln\mathcal{L}_{\rm QSO}$ evaluated with training-fit parameters and fixed training-fit κ_F^*.

2.8. Reproducibility

A self-contained supplementary rerun package implements Unified-Flow distance evaluation, supernova covariance whitening and M-profiling, quasar likelihood with κ_F-profiling, joint optimization, and regeneration of all model-derived figures and tables. The conceptual degeneracy schematic in Figure 1 is a static manuscript illustration assembled directly from the analytic dependencies in Equations (1)–(16).

3. Results

3.1. Dataset Integrity Checks

Supernovae. The Pantheon+SH0ES sample contains $N_{\rm SN} = 1701$ objects with $(z_{\rm HD}, \mu_{\rm SH0ES})$ and the full STAT+SYS covariance matrix $\mathbf{C}_{\rm SN}$. The covariance is symmetric to machine precision and is positive definite, as indicated by a successful Cholesky factorization with strictly positive diagonal entries.

Quasars. The Lusso et al. sample contains $N_{\rm QSO} = 2421$ objects spanning $z \in [0.009, 7.5413]$. The likelihood inputs $(z, \log F_{\rm UV}, \log F_X)$ and their reported measurement uncertainties $(\sigma_{\log F_{\rm UV}}, \sigma_{\log F_X})$ are present for all objects. Group counts were $(\mathrm{G1}, \mathrm{G2}, \mathrm{G3}, \mathrm{G4}, \mathrm{G5}, \mathrm{G6}, \mathrm{G7}) = (14, 1, 35, 106, 1644, 608, 13)$.

3.2. Supernova-Only Anchor Fits

A constant-β supernova-only fit (profiling M analytically) yielded $\beta = -0.49752$ with $\chi^2_{\rm SN} = 1751.82$ and $M^* = 43.0902$, with a one-parameter $\Delta\chi^2 = 1$ interval $\sigma_\beta = 0.01896$. These values reproduce the supernova-only anchor defined in the Unified-Flow framework [1] and are used below for strict low-redshift quasar calibration.

A two-regime step $\beta(z)$ supernova-only fit gave $(\beta_{\rm low}, \beta_{\rm high}, z_t) = (-0.50803, 0.85034, 1.10897)$ with $\chi^2_{\rm SN} = 1747.35$, improving the supernova-only statistic by $\Delta\chi^2 = 4.47$ for two additional parameters.

3.3. Joint Pantheon+SH0ES + quasar fits: Models A–D

Best-fit parameters and 1σ uncertainties are reported in Table 1. All models used analytic profiling of (M, κ_F) and a fitted quasar intrinsic scatter $\sigma_{\rm int}$. Fit statistics and information criteria are given in Table 2. The implied dimensionless distance-modulus curves and separations are shown in Figures 2 and 3. Supernova residual structure for the constant-β and step-$\beta(z)$ anchor fits is shown in Figure 4.

 doi:10.20944/preprints202603.1595.v1

Table 1. Best-fit parameters. Uncertainties for free parameters are 1σ local-quadratic estimates; uncertainties for profiled offsets M and κ_F are conditional profile standard errors evaluated at the best-fit free parameters. Parameters not present in a model are marked "—".

Model	β or $\beta_{\rm low}$	$\beta_{\rm high}$	z_t	γ or γ_0	γ_1	$\sigma_{\rm int}$	M	κ_F
A	−0.46060	—	—	0.67811	—	0.23149	43.1013	−12.5498
	±0.01890			±0.00747		±0.00356	±0.00364	±0.00490
B	−0.50626	14.3310	1.21401	0.617267	—	0.22576	43.0897	−14.2225
	±0.01977	±15.7871	±0.09032	±0.009347		±0.00347	±0.00364	±0.00478
C	−0.49641	—	—	0.58792	−0.01109	0.22491	43.0906	−15.2154
	±0.01893			±0.01042	±0.00094	±0.00346	±0.00364	±0.00476
D	−0.50998	0.95282	1.0772	0.58507	−0.00778	0.22417	43.0874	−15.2376
	±0.01961	±0.645	±0.128	±0.01044	±0.00122	±0.00345	±0.00364	±0.00475

Table 2. Fit statistics and information criteria for Models A–D. Values of $-2\ln\mathcal{L}_{\rm tot}$ are reported up to an arbitrary additive constant from the likelihood normalization; differences are invariant under that constant. Parameter counts include profiled (M, κ_F).

Model	$\chi^2_{\rm SN}$	$\chi^2_{\rm QSO}$	$-2\ln\mathcal{L}_{\rm tot}$	k	AIC	BIC
A	1755.59	2393.93	−2722.36	5	−2712.36	−2680.74
B	1761.93	2387.36	−2836.45	7	−2822.45	−2778.18
C	1751.82	2391.10	−2861.13	6	−2849.13	−2811.19
D	1747.49	2391.03	−2880.08	8	−2864.08	−2813.48

The fitted parameters already separate the low- and high-redshift behavior. Models C and D leave the low-redshift distance law close to the supernova-only anchor, with $\beta \simeq -0.50$ or $\beta_{\rm low} \simeq -0.51$, indicating that adding quasars does not materially perturb the low-z calibration. The principal difference lies in the treatment of the high-z residual trend: if γ is held constant, the fit shifts the cosmological sector toward an extreme $\beta_{\rm high}$, whereas allowing $\gamma_1 < 0$ transfers part of that trend into mild quasar standardization evolution. The cosmological interpretation is therefore not a wholesale re-fitting of the low-z distance scale, but a redistribution of high-z structure between distance-law evolution and quasar evolution.

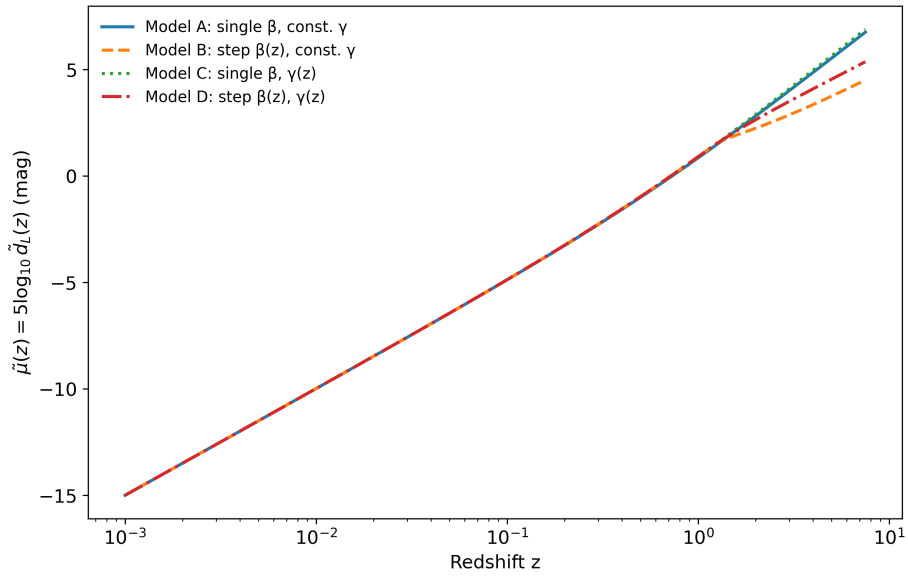

Figure 2. Dimensionless distance modulus $\tilde{\mu}(z) \equiv 5\log_{10}\tilde{d}_L(z)$ versus redshift, with $\tilde{d}_L(z) = (1+z)\int_0^z (1+z')^{-3/2}\phi(z')^{-3/2}\,dz'$. Curves correspond to Models A–D using best-fit β-parameters: Model A $\beta = -0.4606$; Model B $(\beta_{\rm low}, \beta_{\rm high}, z_t) = (-0.5063, 14.33, 1.214)$; Model C $\beta = -0.4964$; Model D $(\beta_{\rm low}, \beta_{\rm high}, z_t) = (-0.5100, 0.9528, 1.077)$.

 doi:10.20944/preprints202603.1595.v1

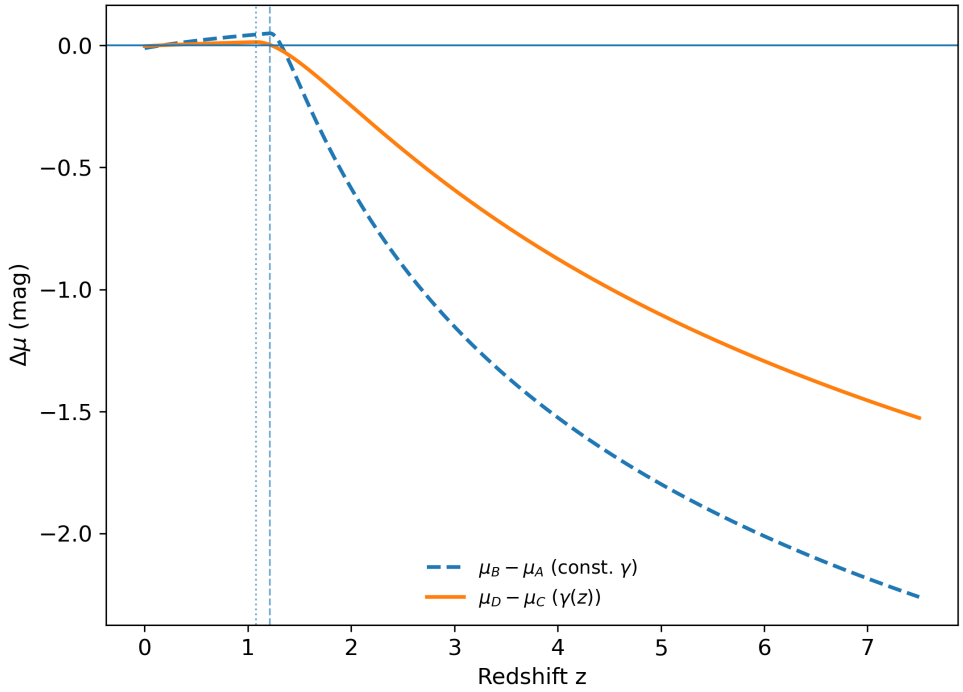

Figure 3. Distance-modulus separation $\Delta\mu(z)$ between step and single distance laws: $\Delta\mu(z) = \mu_{\rm step}(z) - \mu_{\rm single}(z)$, with $\mu(z) = 5\log_{10}\tilde{d}_L(z) + M$ and M profiled analytically from the full Pantheon+SH0ES covariance at fixed distance-law parameters. Shown are $\mu_{\rm B} - \mu_{\rm A}$ (constant γ) and $\mu_{\rm D} - \mu_{\rm C}$ ($\gamma(z)$). Vertical lines mark transition redshifts z_t for Models B and D.

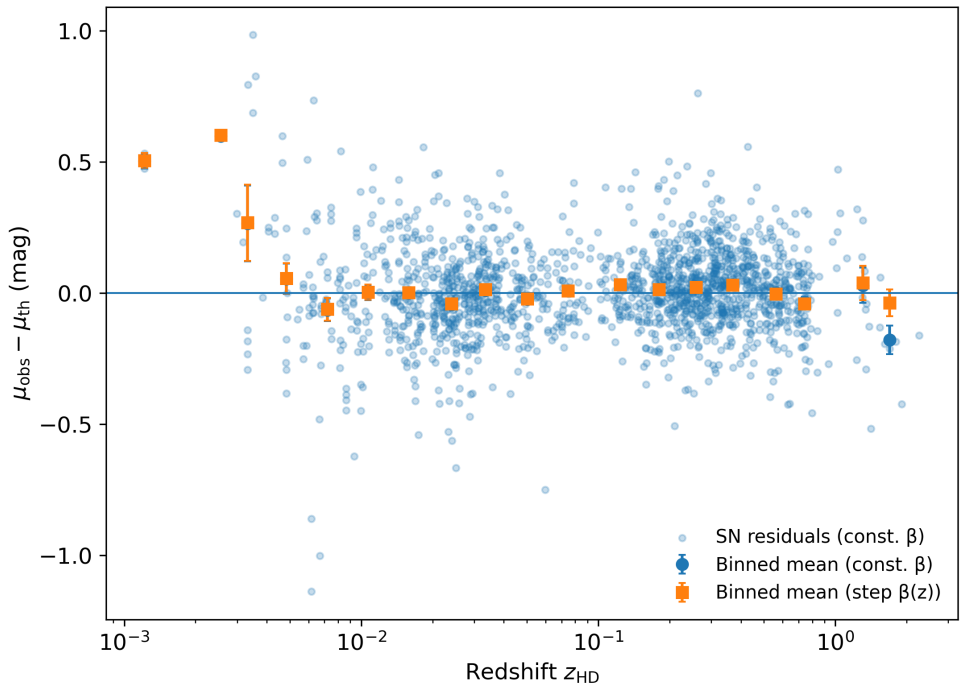

Figure 4. Pantheon+SH0ES supernova residuals $\mu_{\rm SH0ES} - \mu_{\rm th}$ versus $z_{\rm HD}$ ($N_{\rm SN} = 1701$). Gray points show individual residuals for the supernova-only constant-β fit ($\beta = -0.4975$) with analytic profiling of M. Overplotted binned mean residuals ($\pm$ standard error of the mean) compare the constant-β fit (circles) to the supernova-only step-$\beta(z)$ fit (squares) with $(\beta_{\rm low}, \beta_{\rm high}, z_t) = (-0.5080, 0.8503, 1.1090)$.

 doi:10.20944/preprints202603.1595.v1

3.4. Nested Likelihood Tests and Model Preference

Nested likelihood tests favored Model D overall, but the strength of that preference depends on whether $\gamma(z)$ evolution is already admitted. Table 3 reports both likelihood-ratio tail probabilities and the BIC-based Bayes-factor approximation.

Table 3. Nested likelihood-ratio comparisons among the four model classes. Positive ΔBIC values favor the more complex model; $\mathcal{B}_{\rm BIC} \approx \exp(\Delta{\rm BIC}/2)$ is the corresponding large-sample Bayes-factor approximation.

Comparison	$\Delta(-2\ln\mathcal{L})$	Δk	$p_{\rm LR}$	ΔBIC	$\mathcal{B}_{\rm BIC}$
B vs. A	114.09	2	1.68×10^{-25}	97.44	1.44×10^{21}
C vs. A	138.77	1	4.95×10^{-32}	130.45	2.12×10^{28}
D vs. B	43.63	1	3.97×10^{-11}	35.30	4.63×10^{7}
D vs. C	18.94	2	7.71×10^{-5}	2.30	3.14

The comparisons show that introducing either a step in $\beta(z)$ under constant γ or a one-parameter $\gamma(z)$ evolution under single-β produces overwhelming likelihood improvement. By contrast, once $\gamma(z)$ evolution is already present, the residual preference for a step in $\beta(z)$ is statistically real but much smaller: D vs. C still gives $p_{\rm LR} = 7.71 \times 10^{-5}$, yet the BIC-based evidence ratio is only about 3:1. That is the quantitative sense in which the additional distance-law complexity remains modest after slope evolution is admitted.

3.5. Parameter-Correlation Analysis of the Beta(z)–Gamma(z) Degeneracy

The local covariance structure quantifies how the likelihood ridge rotates once quasar evolution is admitted. Table 4 lists the strongest transformed-space correlations extracted from the finite-difference Hessian at the best fit; the full covariance and correlation matrices for Models B and D are included in the supplementary rerun package.

Table 4. Selected local parameter correlations for the step models. Correlations are computed from the transformed covariance matrices used to report the parameter uncertainties.

Model	Parameter 1	Parameter 2	ρ
B	$\beta_{\rm high}$	z_t	$+0.892$
B	$\beta_{\rm high}$	γ	-0.214
D	$\beta_{\rm high}$	z_t	$+0.648$
D	$\beta_{\rm high}$	γ_1	$+0.575$
D	γ_0	γ_1	$+0.468$

The constant-γ step model therefore contains a near-ridge between the amplitude of the high-z step and the location of the transition. Once $\gamma(z)$ is admitted, that extreme ridge weakens, but a moderate trade-off remains between $\beta_{\rm high}$ and γ_1: a steeper high-z distance compression can still be partially exchanged against stronger slope evolution. This is the covariance-level expression of the identifiability problem sketched in Figure 1.

3.6. Extreme Beta_high Behavior Under Constant Gamma

Model B reproduced an extreme high-redshift exponent $\beta_{\rm high} = 14.3310 \pm 15.7871$ with transition $z_t = 1.21401 \pm 0.09032$. Relative to the single-β constant-γ extrapolation (Model A), the implied high-z distance-modulus separation (using each model's profiled M^*) was

$$\Delta\mu(z) \equiv \mu_{\rm B}(z) - \mu_{\rm A}(z) = \begin{cases} -1.152\ {\rm mag}, & z = 3, \\ -1.798\ {\rm mag}, & z = 5, \\ -2.184\ {\rm mag}, & z = 7. \end{cases} \tag{21}$$

 doi:10.20944/preprints202603.1595.v1

The high-redshift residual-drift diagnostic on the $z > 2.3$ subset (ordinary least squares of flux residuals r_i against $u \equiv \ln(1+z)$) gave $dr/du = 0.141 \pm 0.063$ for Model A and $dr/du = -0.022 \pm 0.062$ for Model B, indicating elimination of statistically significant high-z drift by the step-$\beta(z)$ modification when γ is held constant (Figure 5).

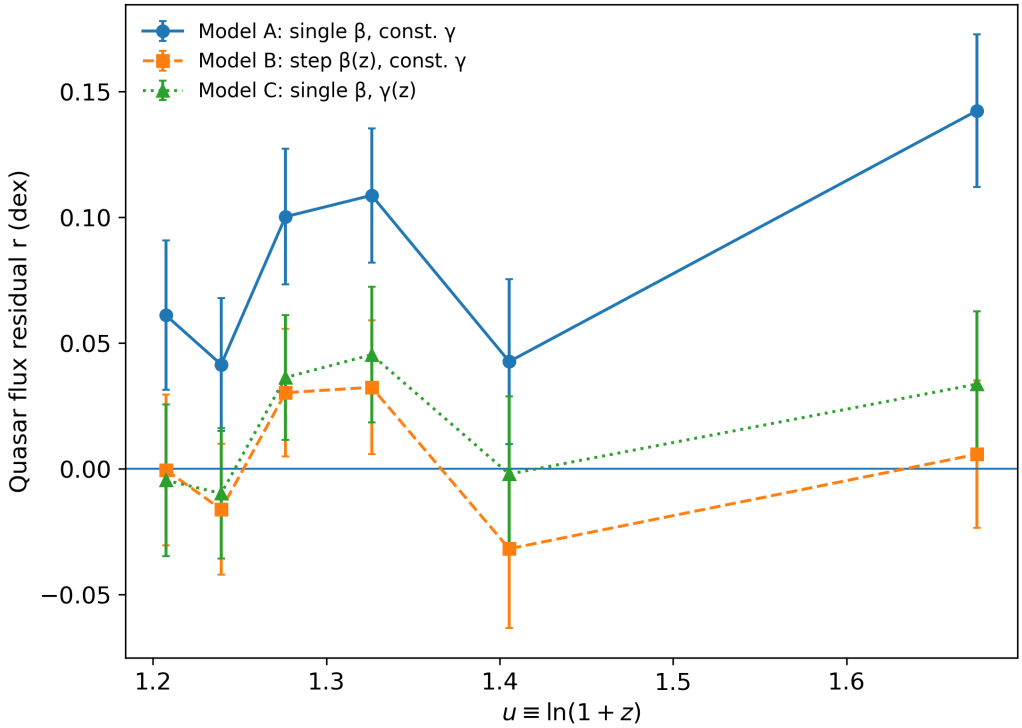

Figure 5. High-redshift quasar residual-drift diagnostic for $z > 2.3$ ($N = 326$). Residuals are $r = \log F_X - \gamma(z) \log F_{\rm UV} - 2(\gamma(z)-1)\log_{10} \tilde{d}_L(z) - \kappa_F$, with κ_F profiled analytically at fixed $(\theta, \gamma, \sigma_{\rm int})$. Binned mean residuals ($\pm$ standard error) are shown versus $u \equiv \ln(1+z)$ for Models A (single β, constant γ), B (step $\beta(z)$, constant γ), and C (single β, $\gamma(z)$). Ordinary-least-squares slopes dr/du on the unbinned subset are $+0.141 \pm 0.063$ (A), -0.022 ± 0.062 (B), and $+0.021 \pm 0.061$ (C).

3.7. Degeneracy Control: Admitting Mild Gamma(z) Evolution

Allowing minimal $\gamma(z) = \gamma_0 + \gamma_1 \ln(1+z)$ evolution collapsed the inferred high-z step from extreme to mild. Model D yielded $\beta_{\rm high} = 0.9528 \pm 0.6448$ with $z_t = 1.0772 \pm 0.1277$ and $\gamma_1 = -0.00778 \pm 0.00122$, corresponding to $\Delta\gamma \simeq -0.016$ from $z = 0$ to $z = 7$ (Figure 6).

The high-z distance-modulus separation between the two $\gamma(z)$ models (Model D relative to Model C) was

$$\Delta\mu(z) \equiv \mu_{\rm D}(z) - \mu_{\rm C}(z) = \begin{cases} -0.592 \text{ mag}, & z = 3, \\ -1.104 \text{ mag}, & z = 5, \\ -1.455 \text{ mag}, & z = 7. \end{cases} \tag{22}$$

This quantitatively demonstrates that the extreme $\beta_{\rm high}$ branch is not robust to admitting mild $\gamma(z)$ evolution. The fitted values have a direct cosmological interpretation. In Models C and D, the low-redshift exponent remains anchored near the supernova-only value, so the joint fit does not require a major revision of the low-z Unified-Flow calibration. The main change is confined to $z \gtrsim 1$, where constant γ would otherwise force a pathologically strong suppression of c/H. Allowing $\gamma_1 < 0$ reassigns part of that apparent geometric compression to mild evolution in the quasar disc–corona standardization itself.

 doi:10.20944/preprints202603.1595.v1

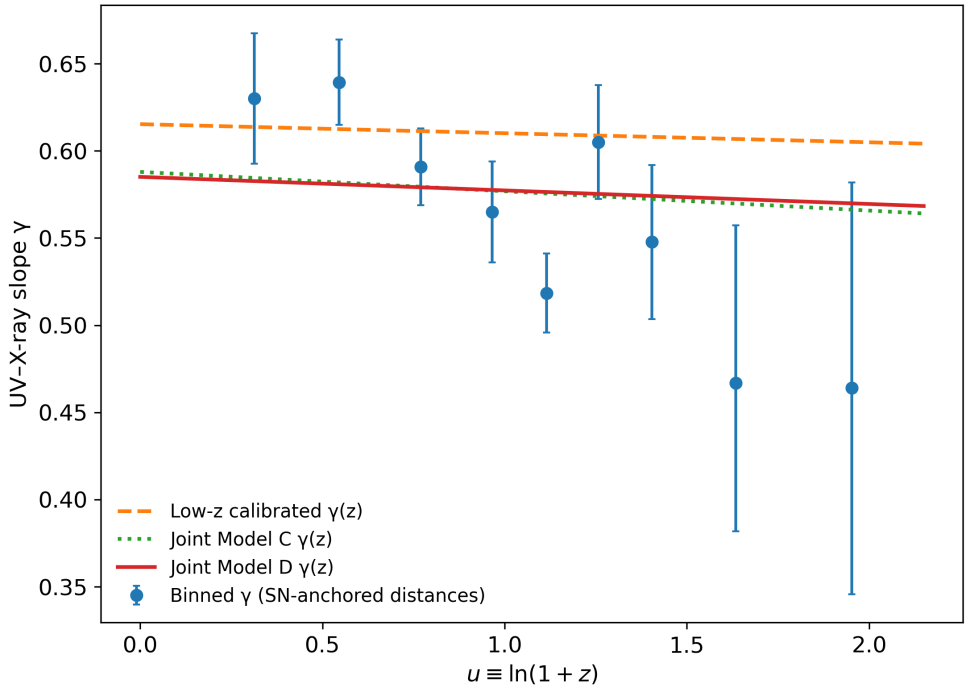

Figure 6. Redshift evolution of the UV–X-ray slope $\gamma(z)$. Points show maximum-likelihood estimates of a constant γ within redshift bins, using supernova-anchored distances from the supernova-only best-fit $\beta = -0.4975$; error bars denote $\Delta(-2\ln\mathcal{L}) = 1$ intervals for one parameter. Lines show $\gamma(z) = \gamma_0 + \gamma_1 \ln(1+z)$ for (i) low-z calibrated $\gamma(z)$ on $z \leq 1.5$ quasars ($(\gamma_0, \gamma_1) = (0.6153, -0.005204)$), and (ii) joint-fit Models C ($(\gamma_0, \gamma_1) = (0.5879, -0.01109)$) and D ($(\gamma_0, \gamma_1) = (0.5851, -0.00778)$).

Information-criterion comparisons are summarized in Figure 7.

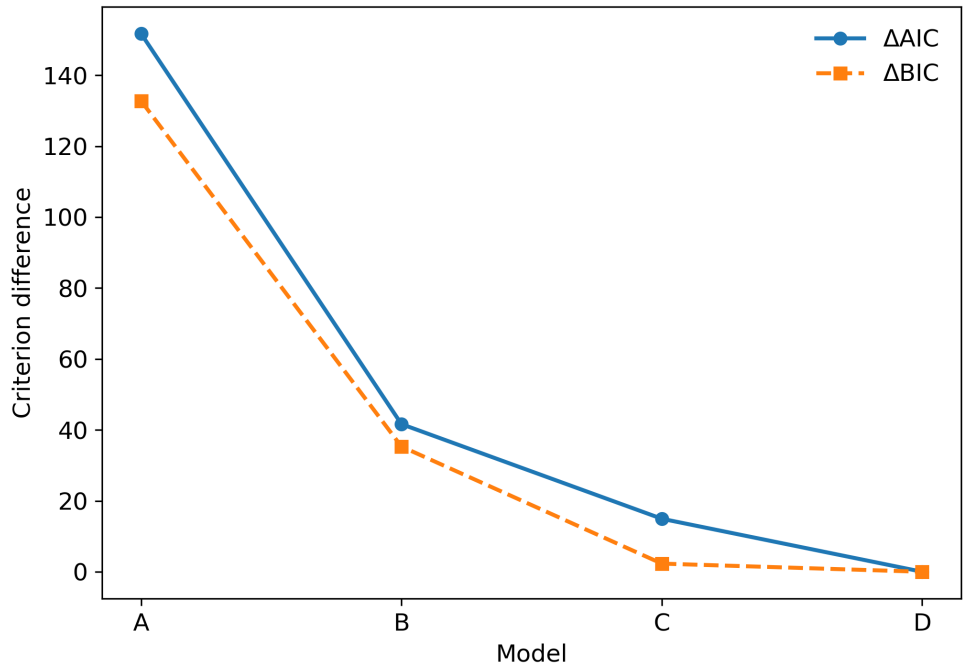

Figure 7. Information-criterion comparison for Models A–D, plotted as ΔAIC and ΔBIC relative to the best model (minimum criterion value). Criteria are AIC $= (-2\ln\mathcal{L}_{\min}) + 2k$ and BIC $= (-2\ln\mathcal{L}_{\min}) + k\ln N$ with $N = N_{\rm SN} + N_{\rm QSO} = 4122$. Parameter counts include profiled (M, κ_F): $k = \{5, 7, 6, 8\}$ for $\{\mathrm{A}, \mathrm{B}, \mathrm{C}, \mathrm{D}\}$.

 doi:10.20944/preprints202603.1595.v1

3.8. Strict Low-Redshift Calibration Test

A strict low-redshift calibration was applied with a calibration subset $z \leq 1.5$ ($N = 1420$), using supernova-only constant-β distances as the anchor.

Table 5. Strict low-redshift quasar calibration and high-redshift inference summary. Calibration uses $z \leq 1.5$ quasars with supernova-anchored distances. Inference fits Unified-Flow distance-law parameters using supernovae and $z > 1.5$ quasars with calibrated quasar parameters held fixed.

Calibration	γ model	Calibrated parameters	$\sigma_{\rm int}$	Inference single-β	Inference step $(\beta_{\rm low}, \beta_{\rm high}, z_t)$	Step gain $\Delta(-2\ln\mathcal{L})$
Low-z	const. γ	$\gamma = 0.64337$	0.23712	$\beta = -0.48508$	(-0.50842, 3.64575, 1.27799)	39.34
Low-z	$\gamma(z)$	$(\gamma_0, \gamma_1) = (0.61530, -0.005204)$	0.23614	$\beta = -0.48765$	(-0.50859, 1.06879, 1.11373)	22.39

Under strict calibration, the inferred high-z step remains mild once $\gamma(z)$ evolution is admitted ($\beta_{\rm high} \approx 1.07$), consistent with collapse of the extreme $\beta_{\rm high}$ regime.

3.9. Predictive Validation by Leakage-Free Quasar Cross-Validation

Cross-validation scores are reported in Table 6 as sums of held-out $-2\ln\mathcal{L}_{\rm QSO,test}$ across folds; positive Δ indicates predictive preference for the step-$\beta(z)$ model.

Table 6. Leakage-free quasar predictive validation summary. Reported values are held-out improvements $\Delta \equiv \sum(-2\ln\mathcal{L}_{\rm QSO,test})_{\rm single} - \sum(-2\ln\mathcal{L}_{\rm QSO,test})_{\rm step}$; $\Delta > 0$ favors a step in $\beta(z)$.

Scheme	Δ (const. γ)	Δ ($\gamma(z)$)
10-fold random	120.08	14.77
10-block redshift	124.55	29.62
High-z holdout ($z \leq 2.3$ train, $z > 2.3$ test)	82.13	13.12

Predictive gains from a $\beta(z)$ step are large and robust when γ is forced constant but become modest when $\gamma(z)$ evolution is allowed, consistent with a distance-law–standardization degeneracy. The impact on cosmological inference is clearest in the high-z holdout. For the $N = 326$ quasars with $z > 2.3$, the constant-γ step model improves the test score by $\Delta = 82.13$, corresponding to about 0.252 units of $-2\ln\mathcal{L}$ per held-out quasar. After admitting $\gamma(z)$, the same comparison falls to $\Delta = 13.12$, or about 0.040 per object. The predictive benefit of a step in the distance law therefore remains real but becomes small enough that the inferred high-z compression is no longer a uniquely preferred cosmological conclusion. Figure 8 summarizes these results.

 doi:10.20944/preprints202603.1595.v1

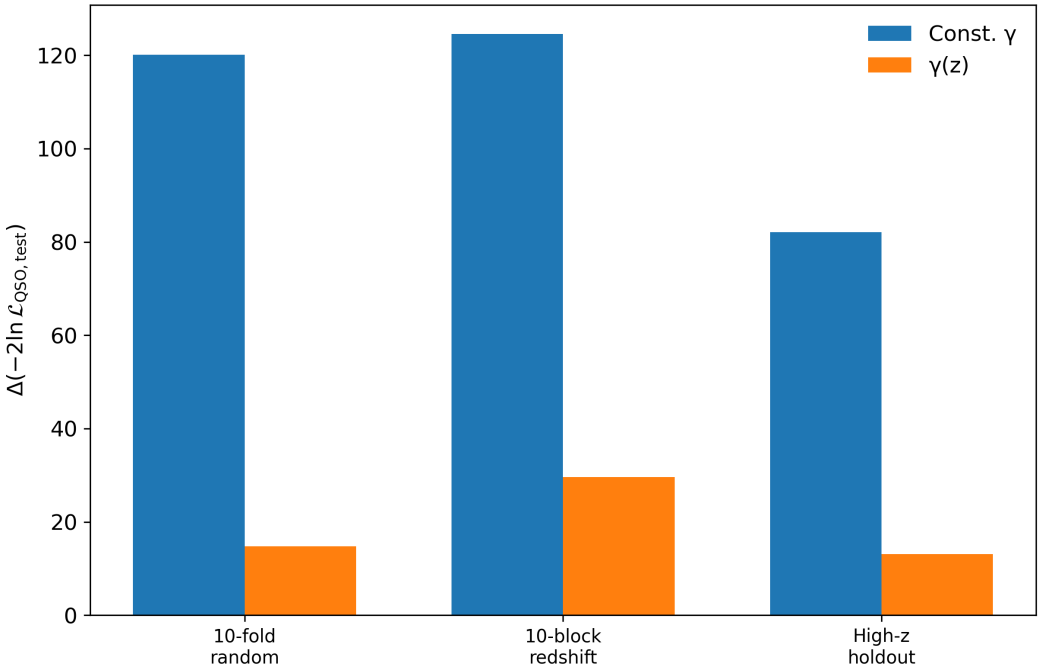

Figure 8. Leakage-free quasar predictive validation summary. Bars show held-out improvement $\Delta(-2\ln \mathcal{L}_{\mathrm{QSO,test}})$ between single-β and step-$\beta(z)$ distance laws (positive values favor step) under constant γ and under $\gamma(z)$, for: 10-fold random cross-validation, 10 contiguous redshift-block cross-validation, and high-z holdout (train $z \leq 2.3$, test $z > 2.3$).

The fitted scaling field $\phi(z)$ and the corresponding light-propagation integrand are shown in Figures 9 and 10.

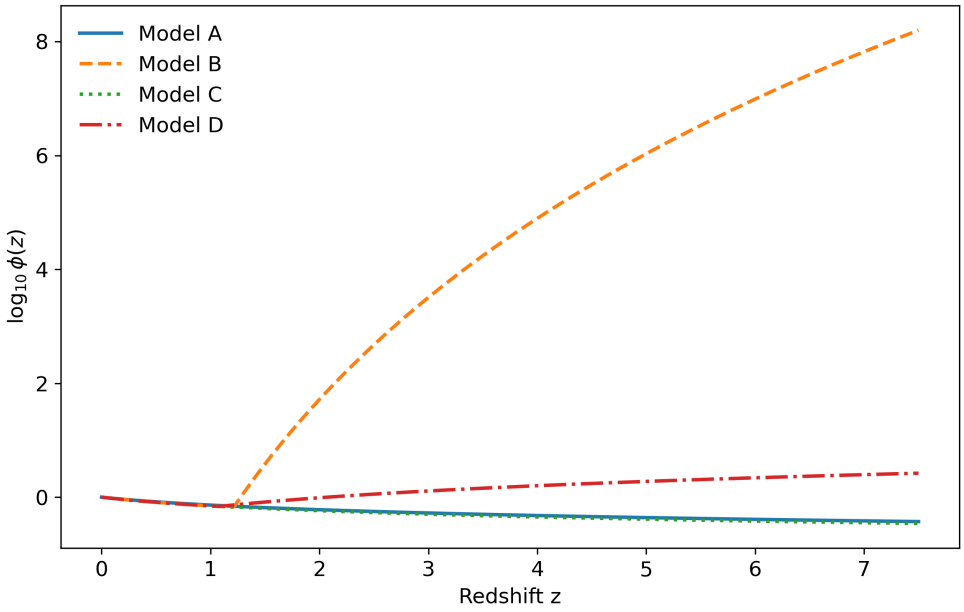

Figure 9. Scaling field $\phi(z)$ for Models A–D, plotted as $\log_{10}\phi(z)$ with normalization $\phi(0) = 1$. For step models, continuity is enforced by $\phi(z) = (1+z)^{\beta_{\mathrm{low}}}$ for $z \leq z_t$ and $\phi(z) = (1+z_t)^{\beta_{\mathrm{low}}-\beta_{\mathrm{high}}}(1+z)^{\beta_{\mathrm{high}}}$ for $z > z_t$. Under the Unified-Flow mapping, the effective light speed scales as $c(z)/c_0 = \phi(z)^{-1}$, so rapid growth of ϕ corresponds to progressively stronger suppression of the light-propagation scale. Model B grows to $\phi(z = 7) \approx 6.6 \times 10^7$, which enforces the extreme compressed-distance branch, whereas Model D reaches only $\phi(z = 7) \approx 2.5$ and therefore represents a mild rather than catastrophic high-z modification.

 doi:10.20944/preprints202603.1595.v1

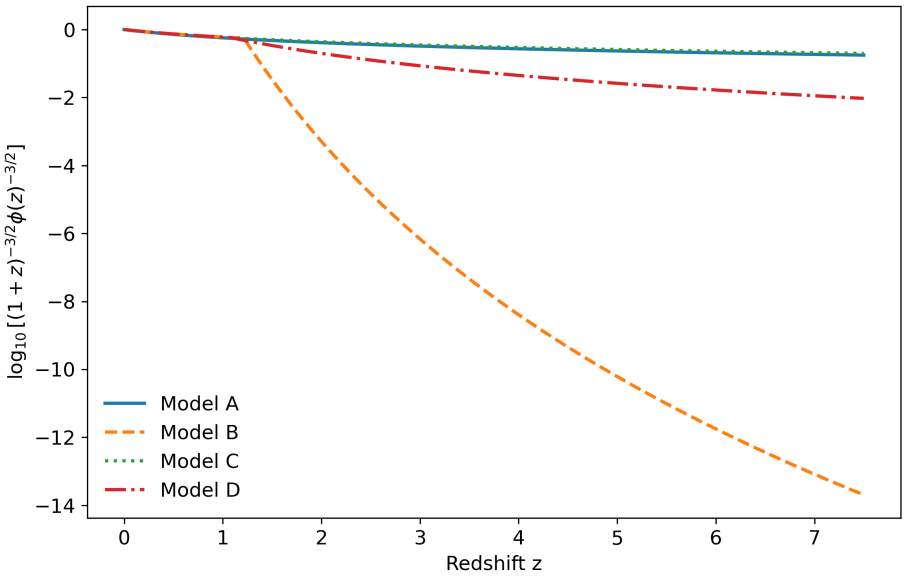

Figure 10. Logarithm of the light-propagation integrand entering $\tilde{d}_L(z)$: $I(z) = (1+z)^{-3/2}\phi(z)^{-3/2}$, shown as $\log_{10} I(z)$ for Models A–D. Strong suppression of $I(z)$ at high redshift corresponds to compression of $\tilde{d}_L(z)$ and hence of $\mu(z)$. The figure shows that Model B drives the integrand down by roughly 13 dex by $z \sim 7$, producing the extreme compressed-distance branch, whereas Model D suppresses the integrand by only about 2 dex and therefore yields a much milder distance compression once $\gamma(z)$ evolution is admitted.

4. Discussion

4.1. Astrophysical Context for the UV–X-Ray Relation and Possible Mild Gamma(z) Evolution

The UV–X-ray relation is physically plausible because both bands arise from the same accretion flow. Thermal optical/UV emission is generated in the disc, while a fraction of those seed photons is inverse-Compton up-scattered in a hot corona into the X-ray band [12,13]. In that picture, the slope γ measures how disc luminosity, coronal power, and radiative geometry covary across the quasar population. Recent disc-illumination calculations reproduce a sublinear UV–X-ray relation when black-hole mass, accretion rate, and the fraction of dissipated power transferred to the corona vary jointly, which makes mild evolution in the observed slope astrophysically admissible rather than ad hoc [44]. Reliability assessments of the cosmological quasar sample likewise emphasize that the main threats to standardization are selection and flux-measurement systematics, not a breakdown of the underlying disc–corona connection [45].

Several mechanisms can generate a weak redshift dependence in $\gamma(z)$ without destroying the usefulness of the relation. Changes in the typical Eddington-ratio distribution, disc temperature, coronal compactness or height, inclination mix, or X-ray bolometric correction can all shift the balance between UV and X-ray output at fixed monochromatic luminosity. The fitted trend reported here, $\Delta\gamma \simeq -0.016$ from $z = 0$ to $z = 7$, is small enough to be compatible with such population-level evolution while remaining large enough to matter for cosmological inference because the quasar likelihood multiplies $\gamma(z) - 1$ by $\log_{10} \tilde{d}_L(z)$ over thousands of objects.

4.2. Empirical Identifiability and the Beta(z)–Gamma(z) Degeneracy

The joint Pantheon+SH0ES + quasar fit constrains the Unified-Flow distance integral $\tilde{d}_L(z)$, not $H(z)$ and $c(z)$ separately. In the quasar standardization, the distance enters through the term $2(\gamma(z) - 1)\log_{10} \tilde{d}_L$. Consequently, small redshift-dependent changes in $\gamma(z)$ generate redshift-dependent shifts in predicted $\log F_X$ that can mimic, or partially replace, changes in $\tilde{d}_L(z)$ induced by $\beta(z)$ evolution.

This structure is quantified by the constant-γ step fit (Model B), which drives $\beta_{\rm high}$ to an extreme value and produces $\mathcal{O}(2)$ mag compression in μ by $z \simeq 7$ relative to the single-β extrapolation. The same dataset, analyzed with minimal evolving $\gamma(z)$ (Model D), no longer supports an extreme $\beta_{\rm high}$;

 doi:10.20944/preprints202603.1595.v1

the optimum collapses to $\beta_{\rm high} = \mathcal{O}(1)$ with a mild $\gamma(z)$ trend. The covariance structure of the Model D parameters is consistent with this trade-off; Table 4 shows notable correlations involving $\beta_{\rm high}$, especially with z_t and γ_1, in the local quadratic approximation.

4.3. Why Constant Gamma Drives an Extreme High-Redshift Regime

The constant-γ single-β model exhibits statistically significant high-z residual drift, signaling misspecification in the combined supernova+quasar context when γ is treated as globally constant. Within that restricted model space, the likelihood improves by introducing a second distance-law regime that reduces or removes the drift, yielding large likelihood gains and strong predictive improvements under multiple cross-validation schemes.

The implied Unified-Flow scaling is correspondingly extreme. Under the mapping $c(z)/c_0 = \phi(z)^{-1}$ [1], the Model B best-fit step implies $\phi(z = 7) \sim 6.6 \times 10^7$ and therefore $c(z = 7)/c_0 \sim 1.5 \times 10^{-8}$. Such a branch is admitted by the joint likelihood only under the restrictive hypothesis of a strictly constant quasar UV–X-ray slope.

4.4. Why Gamma(z) Evolution Collapses Beta_high

Allowing $\gamma(z) = \gamma_0 + \gamma_1 \ln(1+z)$ introduces a physically interpretable deformation of the quasar standardization that directly targets the high-z drift. The best-fit $\gamma_1 < 0$ decreases $\gamma(z)$ by $\simeq 0.016$ from $z = 0$ to $z = 7$, changing the distance-coupling coefficient $2(\gamma - 1)$ by $\simeq 0.032$ across the same range. Because this coefficient multiplies $\log_{10} \tilde{d}_L(z)$, even a percent-level change propagates into coherent redshift-dependent shifts in predicted $\log F_X$ across thousands of objects, substantially altering the likelihood balance between distance evolution and quasar evolution.

Model comparison indicates that $\gamma(z)$ evolution is strongly preferred in this dataset (Model C vs. A; Model D vs. B), whereas the incremental evidence for a $\beta(z)$ step after allowing $\gamma(z)$ evolution is modest by BIC. Predictive checks show the same qualitative behavior: step-$\beta(z)$ gains are large when γ is forced constant but become modest under $\gamma(z)$.

The strict low-z calibrated quasar dimensionless Hubble diagram is shown in Figure 11.

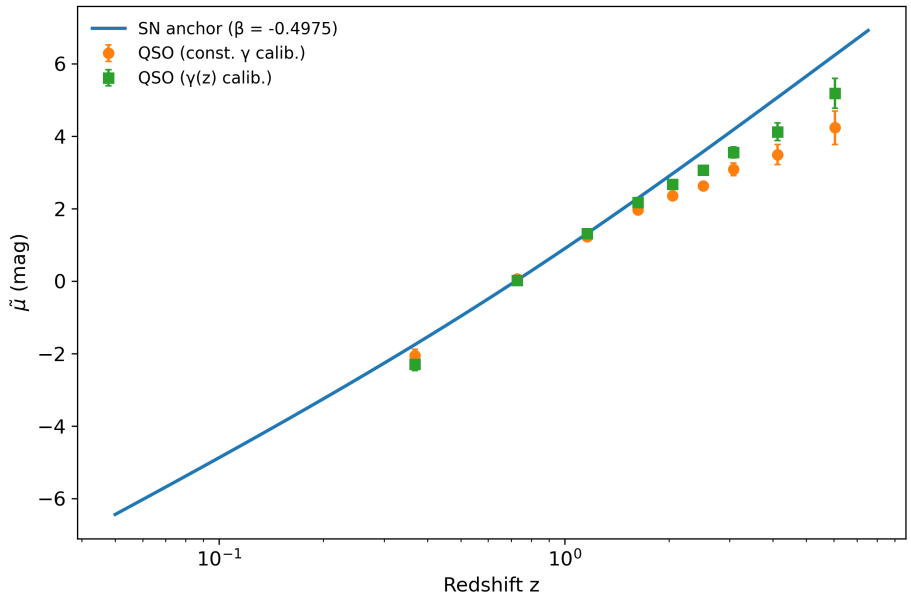

Figure 11. Dimensionless Hubble diagram $\tilde{\mu}(z) = 5\log_{10} \tilde{d}_L(z)$ from supernova-anchored distances and strict low-z quasar calibration. The solid curve is the supernova-anchored prediction for $\beta = -0.4975$. Quasar points show binned $\tilde{\mu}$ inferred by solving the UV–X-ray relation for $\tilde{d}_L$ using parameters calibrated on $z \leq 1.5$ quasars: constant-γ calibration ($\gamma = 0.6434$, $\sigma_{\rm int} = 0.2371$) and evolving $\gamma(z)$ calibration ($\gamma_0 = 0.6153$, $\gamma_1 = -0.005204$, $\sigma_{\rm int} = 0.2361$), with κ_F profiled on the calibration subset. Error bars denote the standard error of the bin mean.

 doi:10.20944/preprints202603.1595.v1

4.5. Role of Strict Low-Redshift Calibration

Strict low-redshift calibration controls leakage of high-z information into quasar standardization parameters. Calibrating $(\gamma, \sigma_{\rm int})$ or $(\gamma_0, \gamma_1, \sigma_{\rm int})$ on $z \leq 1.5$ quasars with supernova-anchored distances prevents the high-z quasar subset from determining $\gamma(z)$. Under this constraint, constant-γ inference still prefers a step in $\beta(z)$ but at a less extreme level, while admitting $\gamma(z)$ again yields a mild step. The calibration results in Table 5 support the conclusion that the extreme $\beta_{\rm high}$ branch is not robust once mild quasar evolution is allowed under leakage control.

4.6. Contextual Comparison to LambdaCDM with Quasar Data

A flat ΛCDM reference curve with Planck 2018 parameters [32] provides a fixed, externally constrained comparison for the dimensionless luminosity distance $\tilde{d}_L(z) = (1+z)\int_0^z dz'/E(z')$. When the quasar UV–X-ray relation is calibrated at low redshift and inverted to infer $\tilde{\mu}(z) = 5\log_{10}\tilde{d}_L(z)$, the resulting high-redshift quasar Hubble diagram deviates systematically from the Planck ΛCDM prediction, consistent with earlier quasar Hubble-diagram analyses [23,25,31]. Figure 12 shows the residual $\Delta\tilde{\mu} \equiv \tilde{\mu}_{\rm QSO} - \tilde{\mu}_{\Lambda\rm CDM}$ for strict low-z calibration of the Lusso et al. catalog. Under constant-γ calibration, the residual trend approaches $\mathcal{O}(1)$ magnitude at $z \gtrsim 4$, while admitting mild $\gamma(z)$ evolution reduces but does not remove the high-z offset.

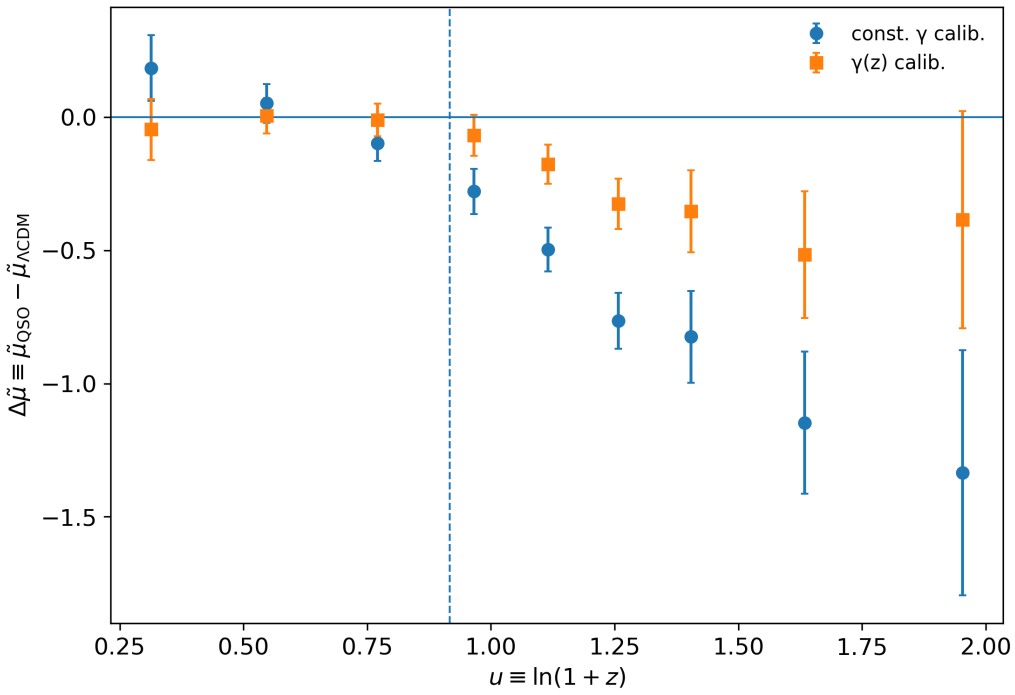

Figure 12. Contextual ΛCDM comparison using a fixed flat ΛCDM reference curve with Planck 2018 matter density $\Omega_m = 0.315$ [32]. Quasar points show binned residuals $\Delta\tilde{\mu} \equiv \tilde{\mu}_{\rm QSO} - \tilde{\mu}_{\Lambda\rm CDM}$ inferred from strict low-z calibration of the UV–X-ray relation on $z \leq 1.5$ quasars. The dashed vertical line marks the calibration boundary at $z = 1.5$.

The comparison is contextual and does not define the primary inference target. The empirically relevant point is that quasar distance indicators continue to provide constraints that are not automatically consistent with standard-model distance curves fixed by external data, motivating models and analyses that treat quasar evolution and distance evolution as simultaneously identifiable hypotheses rather than as fixed assumptions.

 doi:10.20944/preprints202603.1595.v1

4.7. Limitations, Systematic Uncertainties, and Future Tests

1. **Catalog dependence:** the quasar constraints are drawn from a single published catalog realization. Independent catalogs with different selection functions, photometric calibrations, and X-ray reduction pipelines provide a direct test of whether the inferred $\gamma_1 < 0$ trend and the residual preference for a $\beta(z)$ step persist.
2. **High-redshift flux systematics:** at the highest redshifts, rest-frame 2500 Å and 2 keV are inferred from observed bands farther from the target rest frequencies. Spectral extrapolation, flux-limit truncation, and non-simultaneous UV/X-ray variability can therefore introduce redshift-dependent scatter that is only absorbed phenomenologically by $\sigma_{\rm int}$ in the present likelihood.
3. **Model rigidity:** the step form for $\beta(z)$ is a minimal non-smooth deformation. Smooth residual structure in $\log F_X$ could be misallocated between $\beta(z)$ and $\gamma(z)$. This is testable by comparing step versus smooth parameterizations (for example low-order splines) under the same strict calibration protocol and held-out prediction tests.
4. **Observable incompleteness:** only distance-like information is used. Independent observables that constrain quasar spectral-energy-distribution evolution or the disc–corona relation at fixed luminosity would directly break the degeneracy.
5. **Future tests:** decisive discrimination requires independent high-z distance indicators and independent quasar data streams, especially contemporaneous UV/X-ray monitoring, larger spectroscopically validated catalogs, and standard sirens or other high-z candles that bypass quasar standardization.

4.8. Falsifiable Predictions

1. **Redshift trend in the UV–X-ray slope.** Independent quasar catalogs standardized with supernova-anchored distances should prefer $\gamma(z) = \gamma_0 + \gamma_1 \ln(1+z)$ with $\gamma_1 < 0$ and magnitude comparable to $\gamma_1 = -0.00778 \pm 0.00122$ (Model D), corresponding to $\Delta\gamma \simeq -0.016$ between $z = 0$ and $z = 7$.
2. **High-redshift distance-modulus compression under $\gamma(z)$.** When both single-β and step-$\beta(z)$ models allow $\gamma(z)$, the step model should yield $\Delta\mu(z) = \mu_{\rm step} - \mu_{\rm single} < 0$ with $\Delta\mu(3) = -0.592$ mag, $\Delta\mu(5) = -1.104$ mag, and $\Delta\mu(7) = -1.455$ mag for datasets comparable to the Lusso et al. catalog.
3. **High-z residual drift depends on γ rigidity.** For $z > 2.3$, forcing constant γ in a single-β joint fit should yield positive drift $dr/du \approx +0.141 \pm 0.063$, while allowing $\gamma(z)$ should reduce the drift toward zero.
4. **Out-of-sample gain of step-$\beta(z)$ depends on γ rigidity.** For a high-z holdout split (train $z \leq 2.3$, test $z > 2.3$), the held-out improvement should be large if γ is constant ($\Delta \simeq 82.13$ for the Lusso et al. catalog) and modest if $\gamma(z)$ is allowed ($\Delta \simeq 13.12$).
5. **Low-z calibration collapses extreme $\beta_{\rm high}$ if $\gamma(z)$ is admitted.** Under strict low-z calibration, $\beta_{\rm high}$ should remain mild ($\beta_{\rm high} \approx 1.07$) when $\gamma(z)$ is calibrated at low redshift, and should remain far below the extreme constant-γ global-fit value when γ is calibrated constant ($\beta_{\rm high} \approx 3.65$ rather than ~ 14).

Future high-redshift distance indicators, including standard sirens from gravitational-wave observations [46–48], provide independent tests that can break the distance–standardization degeneracy.

5. Conclusions

A joint Pantheon+SH0ES + quasar UV–X-ray analysis within Unified-Flow cosmography identifies Model D as the overall preferred model by likelihood, AIC, and BIC. The more robust physical inference, however, is that allowing mild redshift evolution in the quasar UV–X-ray slope removes the need for the extreme high-redshift branch obtained when γ is forced constant. After admitting $\gamma(z)$ evolution, the preferred step in $\beta(z)$ collapses to an order-unity regime; the additional evidence for Model D over Model C is only modest by BIC, and the held-out predictive gain from a step in $\beta(z)$ becomes small

 doi:10.20944/preprints202603.1595.v1

compared with the constant-γ case. Strict low-redshift calibration and leakage-free cross-validation therefore support mild quasar standardization evolution more robustly than an additional high-redshift distance-law transition. The main limitations are the reliance on a single published quasar catalog, the absence of explicit nuisance parameters for high-redshift flux extrapolation and non-simultaneity, and the rigid step parameterization of $\beta(z)$. The immediate empirical tests are larger independently reduced quasar samples, contemporaneous UV/X-ray spectroscopy, and high-redshift standard candles or standard sirens that probe the distance law without quasar standardization. Within those limits, the present analysis delivers quantitative, falsifiable predictions for independent quasar catalogs and for future high-redshift distance probes.

Author Contributions: Conceptualization, J.Y.; methodology, J.Y.; software, J.Y.; validation, J.Y.; formal analysis, J.Y.; investigation, J.Y.; data curation, J.Y.; writing—original draft preparation, J.Y.; writing—review and editing, J.Y.; visualization, J.Y.

Funding: No external funding was received.

Institutional Review Board Statement: Not applicable.

Informed Consent Statement: Not applicable.

Data Availability Statement: Pantheon+SH0ES and the Lusso et al. quasar catalog are publicly available from the cited sources. The specific tabulations used (Pantheon+SH0ES Hubble-diagram table and covariance matrix; Lusso et al. Table 3 realization) and a self-contained supplementary rerun package required to reproduce the reported results, figures, and tables are provided as supplementary material.

Acknowledgments: The Pantheon+SH0ES collaboration and the quasar-catalog authors are acknowledged for making public data products available.

Conflicts of Interest: The author declares no conflict of interest.

References

1. Yancey, J. *Supernova Hubble Diagram Constraints on a Unified-Flow Model with Redshift-Dependent Fundamental Constants*. Preprints 2026, 2026021100. [https://doi.org/10.20944/preprints202602.1100.v1]
2. Phillips, M.M. The Absolute Magnitudes of Type IA Supernovae. *Astrophys. J. Lett.* **1993**, *413*, L105–L108. https://doi.org/10.1086/186970.
3. Tripp, R. A Two-Parameter Luminosity Correction for Type Ia Supernovae. *Astron. Astrophys.* **1998**, *331*, 815–820. https://ui.adsabs.harvard.edu/abs/1998A%26A...331..815T/abstract.
4. Guy, J.; Astier, P.; Baumont, S.; Hardin, D.; Pain, R.; Regnault, N.; Basa, S.; Carlberg, R.G.; Conley, A.; Fabbro, S.; *et al.* SALT2: Using Distant Supernovae to Improve the Use of Type Ia Supernovae as Distance Indicators. *Astron. Astrophys.* **2007**, *466*, 11–21. https://doi.org/10.1051/0004-6361:20066930.
5. Betoule, M.; Kessler, R.; Guy, J.; Mosher, J.; Hardin, D.; Biswas, R.; Astier, P.; El-Hage, P.; Konig, M.; Kuhlmann, S.; *et al.* Improved Cosmological Constraints from a Joint Analysis of the SDSS-II and SNLS Supernova Samples. *Astron. Astrophys.* **2014**, *568*, A22. https://doi.org/10.1051/0004-6361/201423413.
6. Scolnic, D.M.; Jones, D.O.; Rest, A.; Pan, Y.-C.; Chornock, R.; Foley, R.J.; Huber, M.E.; Kessler, R.; Narayan, G.; Riess, A.G.; *et al.* The Complete Light-curve Sample of Spectroscopically Confirmed SNe Ia from Pan-STARRS1 and Cosmological Constraints from the Combined Pantheon Sample. *Astrophys. J.* **2018**, *859*, 101. https://doi.org/10.3847/1538-4357/aab9bb.
7. Scolnic, D.M.; Brout, D.; Carr, A.; Riess, A.G.; Davis, T.M.; Dwomoh, A.; Jones, D.O.; Ali, N.; Charvu, P.; Chen, R.; *et al.* The Pantheon+ Analysis: The Full Dataset and Light-Curve Release. *Astrophys. J.* **2022**, *938*, 113. https://doi.org/10.3847/1538-4357/ac8b7a.
8. Brout, D.; Scolnic, D.; Popovic, B.; Riess, A.G.; Zuntz, J.; Kessler, R.; Carr, A.; Davis, T.M.; Hinton, S.; Jones, D.O.; *et al.* The Pantheon+ Analysis: Cosmological Constraints. *Astrophys. J.* **2022**, *938*, 110. https://doi.org/10.3847/1538-4357/ac8e04.
9. Riess, A.G.; Yuan, W.; Macri, L.M.; Scolnic, D.; Brout, D.; Casertano, S.; Jones, D.O.; Murakami, Y.; Anand, G.S.; Breuval, L.; *et al.* A Comprehensive Measurement of the Local Value of the Hubble Constant with 1 km s^{-1} Mpc^{-1} Uncertainty from the Hubble Space Telescope and the SH0ES Team. *Astrophys. J. Lett.* **2022**, *934*, L7. https://doi.org/10.3847/2041-8213/ac5c5b.

 doi:10.20944/preprints202603.1595.v1

10. Riess, A.G.; Filippenko, A.V.; Challis, P.; Clocchiatti, A.; Diercks, A.; Garnavich, P.M.; Gilliland, R.L.; Hogan, C.J.; Jha, S.; Kirshner, R.P.; *et al.* Observational Evidence from Supernovae for an Accelerating Universe and a Cosmological Constant. *Astron. J.* **1998**, *116*, 1009–1038. https://doi.org/10.1086/300499.
11. Perlmutter, S.; Aldering, G.; Goldhaber, G.; Knop, R.A.; Nugent, P.; Castro, P.G.; Deustua, S.; Fabbro, S.; Goobar, A.; Groom, D.E.; *et al.* Measurements of Ω and Λ from 42 High-Redshift Supernovae. *Astrophys. J.* **1999**, *517*, 565–586. https://doi.org/10.1086/307221.
12. Haardt, F.; Maraschi, L. A Two-Phase Model for the X-Ray Emission from Seyfert Galaxies. *Astrophys. J. Lett.* **1991**, *380*, L51–L54. https://doi.org/10.1086/186171.
13. Haardt, F.; Maraschi, L. X-Ray Spectra from Two-Phase Accretion Disks. *Astrophys. J.* **1993**, *413*, 507–517. https://doi.org/10.1086/173020.
14. Elvis, M.; Wilkes, B.J.; McDowell, J.C.; Green, R.F.; Bechtold, J.; Willner, S.P.; Oey, M.S.; Polomski, E.; Cutri, R. Atlas of Quasar Energy Distributions. *Astrophys. J. Suppl. Ser.* **1994**, *95*, 1–68. https://doi.org/10.1086/192093.
15. Telfer, R.C.; Zheng, W.; Kriss, G.A.; Davidsen, A.F. The Rest-Frame Extreme-Ultraviolet Spectral Properties of Quasars. *Astrophys. J.* **2002**, *565*, 773–785. https://doi.org/10.1086/324689.
16. Richards, G.T.; Lacy, M.; Storrie-Lombardi, L.J.; Hall, P.B.; Gallagher, S.C.; Hines, D.C.; Fan, X.; Papovich, C.; Siana, B.; Oguri, M.; *et al.* Spectral Energy Distributions and Multiwavelength Selection of Type 1 Quasars. *Astrophys. J. Suppl. Ser.* **2006**, *166*, 470–497. https://doi.org/10.1086/506525.
17. Vignali, C.; Brandt, W.N.; Schneider, D.P. X-Ray Emission from Radio-Quiet Quasars in the Sloan Digital Sky Survey Early Data Release: The α_{ox} Dependence upon Ultraviolet Luminosity. *Astron. J.* **2003**, *125*, 433–443. https://doi.org/10.1086/345973.
18. Steffen, A.T.; Strateva, I.V.; Brandt, W.N.; Alexander, D.M.; Koekemoer, A.M.; Lehmer, B.D.; Schneider, D.P.; Vignali, C. The X-ray-to-Optical Properties of Optically Selected Active Galaxies over Wide Luminosity and Redshift Ranges. *Astron. J.* **2006**, *131*, 2826–2842. https://doi.org/10.1086/503627.
19. Just, D.W.; Brandt, W.N.; Shemmer, O.; Steffen, A.T.; Schneider, D.P.; Chartas, G.; Garmire, G.P. The X-ray Properties of the Most Luminous Quasars from the Sloan Digital Sky Survey. *Astrophys. J.* **2007**, *665*, 1004–1022. https://doi.org/10.1086/519990.
20. Lusso, E.; Comastri, A.; Vignali, C.; Zamorani, G.; Brusa, M.; Gilli, R.; Iwasawa, K.; Salvato, M.; Civano, F.; Elvis, M.; *et al.* The X-ray to Optical-UV Luminosity Ratio of X-ray Selected Type 1 AGN in XMM-COSMOS. *Astron. Astrophys.* **2010**, *512*, A34. https://doi.org/10.1051/0004-6361/200913298.
21. Lusso, E.; Risaliti, G. The Tight Relation between X-ray and Ultraviolet Luminosity of Quasars. *Astrophys. J.* **2016**, *819*, 154. https://doi.org/10.3847/0004-637X/819/2/154.
22. Risaliti, G.; Lusso, E. A Hubble Diagram for Quasars. *Astrophys. J.* **2015**, *815*, 33. https://doi.org/10.1088/0004-637X/815/1/33.
23. Risaliti, G.; Lusso, E. Cosmological Constraints from the Hubble Diagram of Quasars at High Redshifts. *Nat. Astron.* **2019**, *3*, 272–277. https://doi.org/10.1038/s41550-018-0657-z.
24. Lusso, E.; Risaliti, G.; Nardini, E.; Bargiacchi, G.; Benetti, M.; Bisogni, S.; Capozziello, S.; *et al.* Quasars as Standard Candles. III. Validation of a New Sample for Cosmological Studies. *Astron. Astrophys.* **2020**, *642*, A150. https://doi.org/10.1051/0004-6361/202038899.
25. Sacchi, A.; Risaliti, G.; Signorini, M.; Lusso, E.; Nardini, E.; Bargiacchi, G.; Bisogni, S.; Civano, F.; Elvis, M.; Fabbiano, G.; *et al.* Quasars as High-Redshift Standard Candles. *Astron. Astrophys.* **2022**, *663*, L7. https://doi.org/10.1051/0004-6361/202243411.
26. Speri, L.; Tamanini, N.; Caldwell, R.R.; Gair, J.R.; Wang, B. Testing the Quasar Hubble Diagram with LISA Standard Sirens. *Phys. Rev. D* **2021**, *103*, 083526. https://doi.org/10.1103/PhysRevD.103.083526.
27. Trefoloni, B.; Lusso, E.; Nardini, E.; Risaliti, G.; Marconi, A.; Bargiacchi, G.; Sacchi, A.; Pietrini, P.; Signorini, M. Quasars as Standard Candles. VI. Spectroscopic Validation of the Cosmological Sample. *Astron. Astrophys.* **2024**, *689*, A109. https://doi.org/10.1051/0004-6361/202348938.
28. Signorini, M.; Risaliti, G.; Lusso, E.; Nardini, E.; Bargiacchi, G.; Sacchi, A.; Trefoloni, B. Quasars as Standard Candles. IV. Analysis of the X-ray and UV Indicators of the Disc–Corona Relation. *Astron. Astrophys.* **2023**, *676*, A143. https://doi.org/10.1051/0004-6361/202346104.
29. Hu, J.-P.; Wang, F.-Y. High-Redshift Cosmography: Application and Comparison with Different Methods. *Astron. Astrophys.* **2022**, *661*, A71. https://doi.org/10.1051/0004-6361/202142162.
30. Li, X.; Keeley, R.E.; Shafieloo, A.; Zheng, X.; Cao, S.; Biesiada, M.; Zhu, Z.-H. Hubble Diagram at Higher Redshifts: Model Independent Calibration of Quasars. *Mon. Not. R. Astron. Soc.* **2021**, *507*, 919–926. https://doi.org/10.1093/mnras/stab2154.

 doi:10.20944/preprints202603.1595.v1

31. Khadka, N.; Zajaček, M.; Prince, R.; Panda, S.; Czerny, B.; Martínez-Aldama, M.L.; Jaiswal, V.K.; Ratra, B. Quasar UV/X-ray Relation Luminosity Distances Are Shorter than Reverberation-Measured Radius–Luminosity Relation Luminosity Distances. *Mon. Not. R. Astron. Soc.* **2023**, *522*, 1247–1264. https://doi.org/10.1093/mnras/stad1040.
32. Planck Collaboration; Aghanim, N.; Akrami, Y.; Ashdown, M.; Aumont, J.; Baccigalupi, C.; Ballardini, M.; Banday, A.J.; Barreiro, R.B.; Bartolo, N.; *et al.* Planck 2018 Results. VI. Cosmological Parameters. *Astron. Astrophys.* **2020**, *641*, A6. https://doi.org/10.1051/0004-6361/201833910.
33. Eisenstein, D.J.; Zehavi, I.; Hogg, D.W.; Scoccimarro, R.; Blanton, M.R.; Nichol, R.C.; Scranton, R.; Seo, H.-J.; Tegmark, M.; Zheng, Z.; *et al.* Detection of the Baryon Acoustic Peak in the Large-Scale Correlation Function of SDSS Luminous Red Galaxies. *Astrophys. J.* **2005**, *633*, 560–574. https://doi.org/10.1086/466512.
34. Alam, S.; Aubert, M.; Avila, S.; Balland, C.; Bautista, J.E.; Bergé, J.; Bizyaev, D.; Blanton, M.R.; Blomqvist, M.; Bolton, A.S.; *et al.* Completed SDSS-IV Extended Baryon Oscillation Spectroscopic Survey: Cosmological Implications from Two Decades of Spectroscopic Surveys at the Apache Point Observatory. *Phys. Rev. D* **2021**, *103*, 083533. https://doi.org/10.1103/PhysRevD.103.083533.
35. Verde, L.; Treu, T.; Riess, A.G. Tensions between the Early and the Late Universe. *Nat. Astron.* **2019**, *3*, 891–895. https://doi.org/10.1038/s41550-019-0902-0.
36. Di Valentino, E.; Mena, O.; Pan, S.; Visinelli, L.; Yang, W.; Melchiorri, A.; Mota, D.F.; Riess, A.G.; Silk, J. In the Realm of the Hubble Tension—A Review of Solutions. *Class. Quantum Grav.* **2021**, *38*, 153001. https://doi.org/10.1088/1361-6382/ac086d.
37. Powell, M.J.D. An Efficient Method for Finding the Minimum of a Function of Several Variables without Calculating Derivatives. *Comput. J.* **1964**, *7*, 155–162. https://doi.org/10.1093/comjnl/7.2.155.
38. Wilks, S.S. The Large-Sample Distribution of the Likelihood Ratio for Testing Composite Hypotheses. *Ann. Math. Stat.* **1938**, *9*, 60–62. https://doi.org/10.1214/aoms/1177732360.
39. Akaike, H. A New Look at the Statistical Model Identification. *IEEE Trans. Autom. Control* **1974**, *19*, 716–723. https://doi.org/10.1109/TAC.1974.1100705.
40. Schwarz, G. Estimating the Dimension of a Model. *Ann. Stat.* **1978**, *6*, 461–464. https://doi.org/10.1214/aos/1176344136.
41. Kass, R.E.; Raftery, A.E. Bayes Factors. *J. Am. Stat. Assoc.* **1995**, *90*, 773–795. https://doi.org/10.1080/01621459.1995.10476572.
42. Stone, M. Cross-Validatory Choice and Assessment of Statistical Predictions. *J. R. Stat. Soc. Ser. B* **1974**, *36*, 111–147. https://doi.org/10.1111/j.2517-6161.1974.tb00994.x.
43. Arlot, S.; Celisse, A. A Survey of Cross-Validation Procedures for Model Selection. *Stat. Surv.* **2010**, *4*, 40–79. https://doi.org/10.1214/09-SS054.
44. Kammoun, E.; *et al.* Explaining the UV to X-ray Correlation in Active Galactic Nuclei within the Framework of X-ray Illumination of Accretion Discs. *Astron. Astrophys.* **2025**, *697*, A55. https://doi.org/10.1051/0004-6361/202452629.
45. Lusso, E.; *et al.* Are Quasars Reliable Standard Candles? *Astron. Astrophys.* **2025**, *697*, A108. https://doi.org/10.1051/0004-6361/202453504.
46. Schutz, B.F. Determining the Hubble Constant from Gravitational Wave Observations. *Nature* **1986**, *323*, 310–311. https://doi.org/10.1038/323310a0.
47. Holz, D.E.; Hughes, S.A. Using Gravitational-Wave Standard Sirens. *Astrophys. J.* **2005**, *629*, 15–22. https://doi.org/10.1086/431341.
48. Abbott, B.P.; Abbott, R.; Abbott, T.D.; Acernese, F.; Ackley, K.; Adams, C.; Adams, T.; Addesso, P.; Adhikari, R.X.; Adya, V.B.; *et al.* A gravitational-wave standard siren measurement of the Hubble constant. *Nature* **2017**, *551*, 85–88. https://doi.org/10.1038/nature24471.